



Elucidating the promoting role of Mo₂C in methane activation using Ni-_xMo₂C/FAU to catalyze methane steam reforming

Xianghui Zhang ^{a,b}, Kyungmin Yim ^c, Jinsoo Kim ^c, Di Wu ^{a,b,d,e,*}, Su Ha ^{b, **}

^a Alexandra Navrotsky Institute for Experimental Thermodynamics, Washington State University, Pullman, WA 99163, United States

^b The Gene and Linda Voiland School of Chemical Engineering and Bioengineering, Washington State University, Pullman, WA 99163, United States

^c Department of Chemical Engineering (Integrated Engineering), Kyung Hee University, 1732 Deogyeong-daero, Yongin, Gyeonggi-do 17104, South Korea

^d Department of Chemistry, Washington State University, Pullman, WA 99163, United States

^e Materials Science and Engineering, Washington State University, Pullman, WA 99163, United States



ARTICLE INFO

Keywords:

Methane steam reforming (MSR) reaction
Metallic nickel (Ni)
Molybdenum carbide (Mo₂C)
Zeolite Y
Sintering
Coke distribution

ABSTRACT

We report the synthesis and characterization, reaction kinetics, and deactivation mechanism of a series of catalysts with metallic nickel (Ni) and molybdenum carbide (Mo₂C) particles supported on zeolite Y (Ni-Mo₂C/FAU) in methane steam reforming (MSR) reaction at 850 °C. Despite a low Ni loading of 2.4 wt%, MSR on Ni-Mo₂C/FAU exhibits high activity and stability, yet deactivation of Ni-FAU is significant. Further investigations elucidate that the catalyst deactivation is caused by Ni particle sintering via Ostwald ripening instead of coking, and steam induces hydroxylated Ni surface that accelerates sintering. Moreover, Mo₂C boosts the activity and stability of Ni on zeolite Y by enhancing CH₄ activation rather than activating H₂O. The interplays among Mo₂C and Ni particles dynamically balance the carbon formation and consumption rates, and inhibit Ni sintering. This study demonstrates that high MSR activity and stability can be achieved on transition metal carbide – Ni catalysts with systematically tuned compositional, structural, and interfacial factors.

1. Introduction

Hydrogen (H₂) is a critical alternative fuel and a clean energy form that plays an important role in closing the global carbon cycle. [1,2] In the current chemical industry and energy infrastructure, the most hydrogen-dependent processes include ammonia synthesis (55%), refinery (25%), and methanol production (10%). [1,2] With high energy efficiency up to 60% and minimized negative environmental impacts, the hydrogen-based fuel cell is potentially the next major hydrogen consumption process as we drive to a more sustainable future with hydrogen fuel cell electric vehicles (FCEVs). [3,4] Beyond serving as a critical raw material in the chemical industry, H₂ is also a reducing agent in the metallurgical industry. Therefore, efficient catalytic extraction of hydrogen from water, light hydrocarbons, and other organics where hydrogen is chemically stored, as environmental-friendly fuel in large quantity is an essential and crucial step towards a cleaner future. [5].

Currently, methane steam reforming (MSR) is the dominant industry-scale process to produce H₂. Typical industrial MSR reactions are carried out at 800 ~ 1100 °C with pressure between 14 and 40 bar.

MSR is a highly endothermic reaction ($\Delta H_r = 206$ kJ/mol), [6] in which high temperature is a favorable reaction condition to yield a high conversion, especially, at high space velocity. The main challenges of such harsh reaction conditions are coking and sintering of the catalytic Ni-based metallic particles. [7–16] It has been demonstrated that without an excessive amount of water or coking-inhibiting agents, supported Ni catalysts suffer from severe coking in CH₄ reforming. Thus, modifications of the Ni sites are necessary to prevent coke formation. It has been reported that introduction of the second type of metals, such as Ag, Au, Sn, Co, Mo, and Cu, effectively prevents coking through the formation of alloyed Ni nanoparticles (NPs). [6] The introduced metal atoms typically occupy the step sites of Ni NPs, which feature the highest CH₄ decomposition rate, to effectively inhibit coke formation. In these studies, Ni NPs with loading higher than 8 wt% were supported on α -Al₂O₃, which has surface areas lower than 10 m²/g at high temperature. [6,17–20] As a result, the abrupt formation of coke at the catalytic sites may quickly reduce the activity. It also prevents the proper water transport to the catalyst surface, which leads to the uncontrollable growth of carbon filaments. In other words, for effective MSR, catalysts

* Corresponding author at: Alexandra Navrotsky Institute for Experimental Thermodynamics, Washington State University, Pullman, WA 99163, United States.

** Correspondence to: O.H. Reaugh Laboratory for Oil and Gas Research, Washington State University, Pullman, WA 99163, United States

E-mail addresses: d.wu@wsu.edu (D. Wu), suha@wsu.edu (S. Ha).

with high support surface areas and well-dispersed Ni-based catalytic NPs need to be engineered.

Owing to its noble-metal-like physical-chemical properties, Mo_2C has been a popular candidate for heterogeneous catalysis of water-gas shift (WGS) reaction, bio-oil upgrading, and alcohol (methanol and ethanol) steam reforming. [21–24] The common role of Mo_2C in fuel reforming is to prevent coke formation by increasing the activation of oxygen-containing molecules, such as H_2O and CO_2 . Sabinis *et. al.* [25, 26] studied the WGS reaction mechanism of a series of catalysts with transition and noble metals supported on Mo_2C . They concluded that the active sites reside at the metal- Mo_2C interfaces. They also elucidated that for WGS, in reaction at relatively low temperature, the role of Mo_2C is to adsorb and activate H_2O . Yao *et. al.* reported activation of H_2O on raft-like Au clusters supported by $\alpha\text{-MoC}$. [27] Shi *et. al.* studied the catalytic role of Ni/ Mo_2C with different Ni/Mo ratios in dry reforming of methane (DRM), in which they suggested that the activation of CO_2 is on Mo_2C , and CH_4 activation is on Ni NPs. [28] Hence, it is clear that the high coke-resistant of Mo_2C as support originates from its highly efficient roles in activating oxygen-containing molecules.

Hydrocarbon activation using Mo_2C requires closely balanced activity – temperature interplays. Past reaction engineering studies mainly concentrated on temperatures lower than 800 °C, at which the CH_4 activation on Mo_2C was poor. Recently, Bkour *et. al.* performed CH_4 temperature-programmed reaction ($\text{CH}_4\text{-TPR}$) on bulk Mo_2C and unsupported Ni- Mo_2C bimetallic catalysts, in which they found that the onset CH_4 decomposition temperature is around 710 °C on Ni- Mo_2C , and is ~900 °C on bulk Mo_2C . [29] Using Ni- Mo_2C with different Ni/Mo ratios, Yao *et. al.* further pointed out that the CH_4 decomposition rate in $\text{CH}_4\text{-TPR}$ would reach its maximum at a temperature higher than 930 °C. [28] These studies suggest promoting roles of Mo_2C for Ni-based catalysts in MSR, and as the Mo content varies the rate of CH_4 decomposition evolves. Moreover, Mo_2C promotes CH_4 decomposition in high-temperature reactions, while it favors H_2O activation at low temperatures.

This study focuses on the catalytic performance, reaction kinetics, and deactivation mechanism of zeolite Y (faujasite, FAU) with only supported Ni (Ni-FAU) and with both supported Ni and Mo_2C particles (Ni- Mo_2C /FAU) in MSR reaction, in which distinctively different roles of Ni NPs and Mo_2C were elucidated and discussed. Zeolite Y is selected as the support of Ni and Mo_2C species because of its high surface area and effective stabilization of metallic particles, and thermal stability at temperatures higher than 800 °C. Our Ni- Mo_2C /FAU catalysts were characterized using *ex situ* X-ray diffraction (XRD), high-resolution transmission electron microscopy (HRTEM) coupled with an energy-dispersive X-ray analyzer (EDX), and *in situ* CO adsorption diffuse reflectance infrared Fourier transform spectroscopy (DRIFTS). The catalytic performance and kinetic study of MSR over all catalyst samples were investigated using a fixed-bed reactor. Further, coupled with thermal analysis using an integrated thermogravimetry-differential scanning calorimetry-mass spectrometry (TG-DSC-MS) system, we successfully elucidated the deactivation mechanisms, quantified the degree and distribution of coking of spent catalysts after MSR, and distinguished the unique roles of Ni and Mo_2C . Notably, Mo_2C NPs increase the catalytic activity and stability via promoting CH_4 activation instead of H_2O activation. Reaction kinetics with closely balanced CH_4 activation and Ni sintering is necessary to enable MSR with high activity and stability.

2. Experiment methods

2.1. Material synthesis

Zeolite NH_4Y (NH_4^+ -FAU) with Si/Al ratio = 2.9 was purchased from Alfa Aesar. It was calcined at 500 °C in the air for 4 h to convert it into zeolite HY (FAU). Ion exchange was applied to prepare Ni-exchanged zeolite Y (Ni^{2+} -FAU) from NH_4^+ -FAU. Specifically, NH_4^+ -FAU (1.00 g)

was introduced to $\text{Ni}(\text{NO}_3)_2$ aqueous solution (0.25 mol/L, 20 mL). This mixture was kept at 50 °C for 24 h under vigorous stirring. Such an ion-exchange process was triplicated to maximize the degree of Ni-exchange. Eventually, the solid product, denoted as Ni^{2+} -FAU, was washed, oven-dried at 100 °C overnight, and calcined at 500 °C for 4 h. Ni^{2+} -FAU was reduced in pure H_2 at 700 °C for 2 h, leading to the sample with Ni metal, Ni-FAU. Further, Mo precursor was introduced by incipient wetness impregnation (IWI). Before impregnation, Ni-FAU was pretreated under vacuum at 80 °C for 4 h. Then 1.5 mL ammonia molybdate aqueous solution (0.005 – 0.07 mol/L) was added to 1 g of Ni-FAU followed by sonication for 1 h. The product was oven-dried at 100 °C overnight, and calcined at 500 °C for 4 h. Finally, the calcined samples were carburized using a temperature programmed method described by Iida *et. al.* [30] Specifically, each calcined sample was carburized in a stream of CH_4/H_2 gas mixture (15 vol% of CH_4) at a total flow rate of 85 sccm. The temperature was increased to 300 °C at 5 °C/min, and to 700 °C at 1 °C/min, at which carburization lasted for 2 h. The carburized samples were denoted as Ni- $x\text{Mo}_2\text{C}$ /FAU, in which x represents the mass percentage of Mo loading (wt%), ranging from 0.0 to 7.0 wt%.

2.2. Sample characterizations

The Ni concentration on Ni-FAU sample was determined using inductively coupled plasma mass spectrometry (ICP-MS, see Table S1). For phase identification, *ex situ* powder X-ray diffraction (XRD) patterns were collected at room temperature between 5 and 60 ° (2 °/min) on a Rigaku Miniflex 600 diffractometer (40 kV, 15 mA, Cu $\text{K}\alpha$, $\lambda = 0.15418$ nm). Transmission electron microscopy (TEM, FEI Tecnai T20, a LaB₆ cathode at 200 kV) and high-resolution transmission electron microscopy (HRTEM; Tecnai F20 G2, FEI, USA) were employed to reveal the sample morphology and NP size. EDX-elemental mapping was also performed with an Oxford Ultimax detector. Thermal analysis using an integrated TG-DSC-MS system (Netzsch STA 449 F5 Jupiter coupled with a QMS 403 D Aëlos) was performed to elucidate the coking mechanism. In each measurement, about 10 mg of sample was placed in a platinum (Pt) crucible and analyzed from 30 to 700 °C (10 °C/min) under O_2/N_2 gas mixture (10 vol% O_2) at a total flow rate of 60 mL/min. The evolved gases in TG-DSC analysis were simultaneously identified and quantified by the coupled MS. Specifically, the MS signal of CO_2 was normalized based on the weight of the sample loaded in the crucible and deconvoluted using Gaussian distribution. The ratios of “light coke” and “hard coke” were calculated using the areas of deconvoluted peaks (Fig. S10). N_2 adsorption–desorption full isotherm analysis was carried out on selected samples at –196 °C (77 K) using a Micromeritics 3Flex multiport analyzer, in which the sample was outgassed at 350 °C under vacuum for 5 h before each measurement. The isotherm data collected were used to derive the Brunauer–Emmett–Teller (BET) surface area and pore size distribution. The reduction behaviors of each calcined sample were examined by using the temperature-programmed reduction of H_2 ($\text{H}_2\text{-TPR}$) technique on a Diablo 5000 A real-time gas analyzer with an Agilent 5975 C MSD as the detector. Before $\text{H}_2\text{-TPR}$ measurement, each sample, 55 mg, was heated at 500 °C for 0.5 h in argon to remove water. After the pretreatment, the sample was cooled down to room temperature and Ar gas was switched to 50 vol% H_2 /Ar with a total flow rate of 50 mL/min. The sample was heated to 900 °C at a heating rate of 10 °C/min. Water signal during the process was recorded and plotted in Fig. S3.

2.3. *In situ* diffuse reflectance infrared fourier transform spectroscopy (*in situ* DRIFTS)

In situ diffuse reflectance infrared Fourier transform spectroscopy (*in situ* DRIFTS) analysis was carried out using a high-temperature cell (SpectraTech) with ZnSe windows. Prior to each analysis, 25 mg sample was finely ground and placed in a ceramic crucible. Pretreatment was

carried out at 600 °C in pure H₂ gas stream for Ni-FAU, and in CH₄/H₂ (15 vol% CH₄) stream at 50 sccm for 30 min for Ni-xMo₂C/FAU. The background spectrum was collected when the cell was cooled down to room temperature under helium (He) flow. In the *in situ* CO adsorption DRIFTS experiments, the carrier gas was switched to pure CO.

2.4. Catalytic performance test

The catalytic performance of each sample in methane steam reforming (MSR) was tested using a quartz-tube fixed-bed reactor (7-mm). Specifically, the catalyst (~55 mg) was loaded into the reactor with a catalyst bed height of 4 mm. All catalysts were pretreated in CH₄/H₂ stream (15 vol% CH₄) at 700 °C for 30 min. The flow rate of CH₄ stream was programmed at 20 sccm, and the steam-to-carbon ratios (S/C) were set to be either 1.0 or 1.5. Water vapor was introduced to the reactor via a microsyringe pump at 1.0 mL/h (for the S/C ratio = 1.0) and 1.5 mL/h (for the S/C ratio = 1.5). The evolved products were analyzed using an SRI gas chromatograph equipped with a molecular sieve 13X column, a HayeSep D packed column, and a thermal conductivity detector (TCD). The conversion of CH₄ was calculated using Eq. (1). The yields of H₂, CO, and CO₂ were calculated using Eqs. (2), (3), and (4), respectively.

$$CH_4 \text{ conversion} = \frac{\text{moles of } (CH_4 \text{ in} - CH_4 \text{ out})}{\text{moles of } CH_4 \text{ in}} \quad (1)$$

$$H_2 \text{ yield} = \frac{2 \cdot \text{moles of } H_2 \text{ produced}}{4 \cdot \text{moles of } CH_4 \text{ in} + 2 \cdot \text{moles of } H_2O \text{ in}} \quad (2)$$

$$CO \text{ yield} = \frac{\text{moles of } CO \text{ produced}}{\text{moles of } CH_4 \text{ in}} \quad (3)$$

$$CO_2 \text{ yield} = \frac{\text{moles of } CO_2 \text{ produced}}{\text{moles of } CH_4 \text{ in}} \quad (4)$$

2.5. Kinetic analysis

The reaction kinetics were determined using a fixed-bed reactor containing 25 mg of the catalyst under a feed gas stream of CH₄ (20 sccm) and N₂ (10 sccm) to closely mimic a differential reactor with minimized mass transfer limitation. The conversions were controlled below 10% for the determination of kinetic parameters. Except for Ni-FAU, whose deactivation rate is too fast to collect reliable data, all catalysts were tested at S/C ratio = 1.0 and 1.5. The data were recorded between 750 and 900 °C, at which the catalysts remained stable.

2.6. Catalytic performance test with CH₄ pulse reaction

CH₄ pulse reaction experiments were conducted on all samples using a Diablo 5000 A real-time gas analyzer with an Agilent 5975 C MSD as the detector. All samples were pre-heated in CH₄/H₂ (15 vol% CH₄) stream from room temperature to 700 °C at 10 °C/min, and kept at 700 °C for 30 min for surface oxygen removal. Subsequently, the reaction temperature was increased to 850 °C under Ar flow (50 mL/min) before each CH₄ pulse for 10 s followed by Ar purge for 3 min. The flow rates of CH₄ and Ar were 30 mL/min and 50 mL/min, respectively.

3. Results

The ICP-MS data suggest that after ion exchange, the Ni loading is 2.4 wt% for Ni-FAU. The Mo content was determined according to the precursor loading. The XRD patterns plotted in Fig. 1 confirm that all samples retain the cubic structure (*Fd3m*) of zeolite Y after the multistep catalyst synthesis processes. The (111) of metallic Ni at 44.5 ° overlaps with the XRD peak of FAU support. Thus, it cannot be used to determine the presence or to estimate the average crystalline size of Ni. In addition,

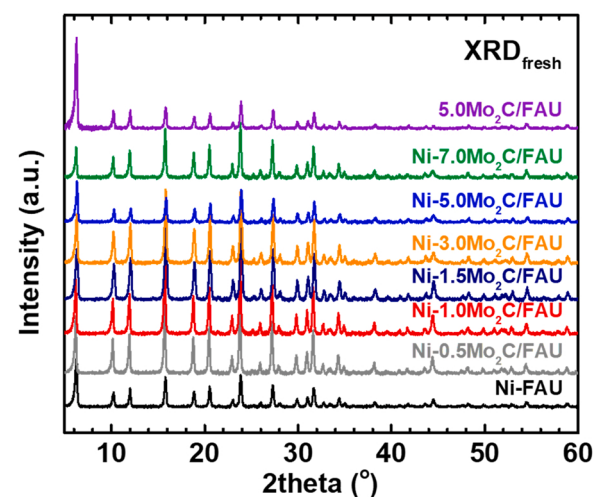


Fig. 1. *Ex situ* XRD patterns of all fresh catalyst samples at room temperature.

at 39.5 ° the peak of Mo₂C (121) plane is not observed, which suggests that the sizes of Mo₂C particles are below the detection limit of typical lab-accessible XRD. The N₂ adsorption and desorption isotherms and pore size distribution of Ni-FAU and Ni-xMo₂C/FAU ($x = 1.0, 3.0$, and 5.0) are plotted in Fig. 2 and also summarized in Table 1. As the Mo loading increases, the internal surface area decreases from $507.9 \text{ m}^2/\text{g}$ for Ni-FAU to $428.8 \text{ m}^2/\text{g}$ for Ni-5.0Mo₂C/FAU. The external surface area and pore size follow the same trend. These results indicate that Mo₂C is distributed both inside and outside the FAU framework. According to the TEM images of Ni-FAU (Fig. S1), there appears to be no detectable NP on the external surface of Ni-FAU, indicative of high Ni dispersion within the framework. For all the Ni-xMo₂C/FAU samples, externally NPs are observed with an average particle size of $\sim 6.6 \text{ nm}$. The population of NPs increases as the Mo loading increases, yet no detectable particle growth was seen until $x = 7.0$. Interestingly, Mo₂C/FAU, the sample without Ni, has no external NP, which is consistent with our previous results. [31] Overall, results from XRD and TEM analyses suggest that for Ni-FAU, the Ni NPs are highly dispersed within the framework, and for Ni-xMo₂C/FAU, NPs were observed on the external surface of FAU and share a similar size of $\sim 6.6 \text{ nm}$.

To identify the chemical natures of particles and to elucidate the distributions of Ni and Mo₂C, we carried out HRTEM and EDX analyses on fresh Ni-FAU and Ni-5.0Mo₂C/FAU (The signals of Si and Al are shown in Fig. S2). In Fig. 3a and b, Ni on Ni-FAU is highly dispersed, which is consistent with the TEM image shown in Fig. S1. The Ni on Ni-5.0Mo₂C/FAU appears to be slightly agglomerated, leading to the formation of Ni NPs. Interestingly, the Mo mapping of Ni-5.0Mo₂C/FAU (Fig. 3f) reveals that Mo is highly dispersed. Since Mo₂C is the thermodynamically favorable phase under the carburization process applied, the Mo element primarily presents as the Mo₂C phase for Ni-5.0Mo₂C/FAU. [32] It is also noticeable that the large Ni NPs on Ni-5.0Mo₂C/FAU are mainly in the regions where the Mo₂C population is low (outside the red dash line). Such a phenomenon indicates the positive roles of Mo₂C in promoting the dispersion of Ni NPs. Overall, the HRTEM and EDX results confirm that the particles observed on the external surface of Ni-5.0Mo₂C/FAU are primarily Ni particles with well-dispersed Mo₂C.

The reduction behaviors of samples were plotted in Fig. S3. The water signal presents two different peaks, indicating two distinctive reduction events. The first water peak appears between 400 and 600 °C, which is due to the reduction of MoO₃, because it is only observed for samples with Mo. The second water peak, not seen for samples with Mo, presents at a temperature higher than 700 °C, which is owing to the reduction of NiO. Under the presence of NiO, the reduction of MoO₃ on FAU shifts from 500 °C to temperatures between 430 and 470 °C. This

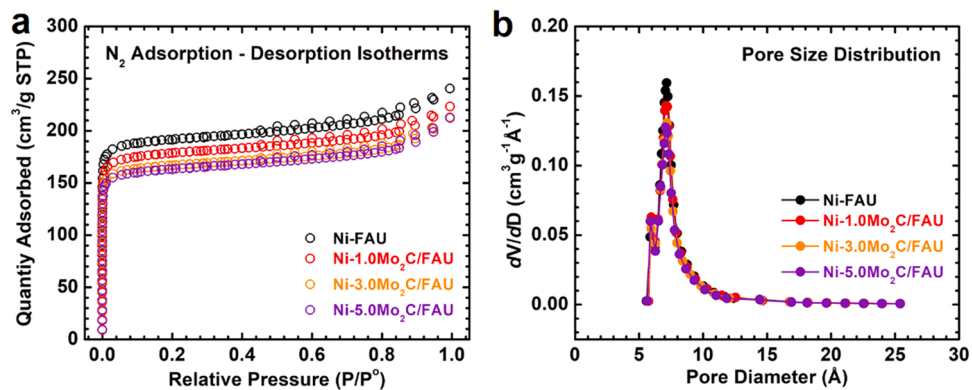


Fig. 2. (a) N_2 adsorption – desorption isotherms and (b) corresponding pore size distribution plots of Ni-FAU and Ni- x Mo₂C/FAU measured at 77 K (-196 °C). $x = 1.0, 3.0$ and 5.0.

Table 1

BET surface areas, pore sizes, and Ni dispersion of Ni-FAU and Ni- x Mo₂C/FAU. $x = 1.0, 3.0$ and 5.0.

| Samples | Surface areas (m ² /g) | | Pore size (Å) | Ni Dispersion (%) |
|-----------------------------|-----------------------------------|----------|---------------|-------------------|
| | Internal | External | | |
| Ni-FAU | 507.9 | 71.5 | 7.20 | 29.2 |
| Ni-1.0Mo ₂ C/FAU | 470.4 | 69.7 | 7.20 | 26.5 |
| Ni-3.0Mo ₂ C/FAU | 441.1 | 65.5 | 7.17 | 28.7 |
| Ni-5.0Mo ₂ C/FAU | 428.8 | 63.5 | 7.15 | 29.8 |

phenomenon highlights the influence of Ni on the redox property of MoO₃.

H₂ chemisorption was also conducted on four selected samples to elucidate the impact of Mo₂C loadings on Ni dispersion (see Table 1). The dispersion of Ni on Ni-FAU is ~ 29.2%. The initial introduction of Mo₂C leads to decreased Ni dispersion. As the Mo₂C content increases, the Ni dispersion trend is switched to an increase as a function of Mo₂C loading. Without sufficient stabilization from enough Mo₂C particles, the initial reduction of Ni dispersion at low Mo₂C loading is due to a much longer heating time used in the carburization process for example, 635 min for Ni- x Mo₂C/FAU samples compared with 180 min for Ni-FAU. As the Mo₂C loading increases, the thermal stability of Ni

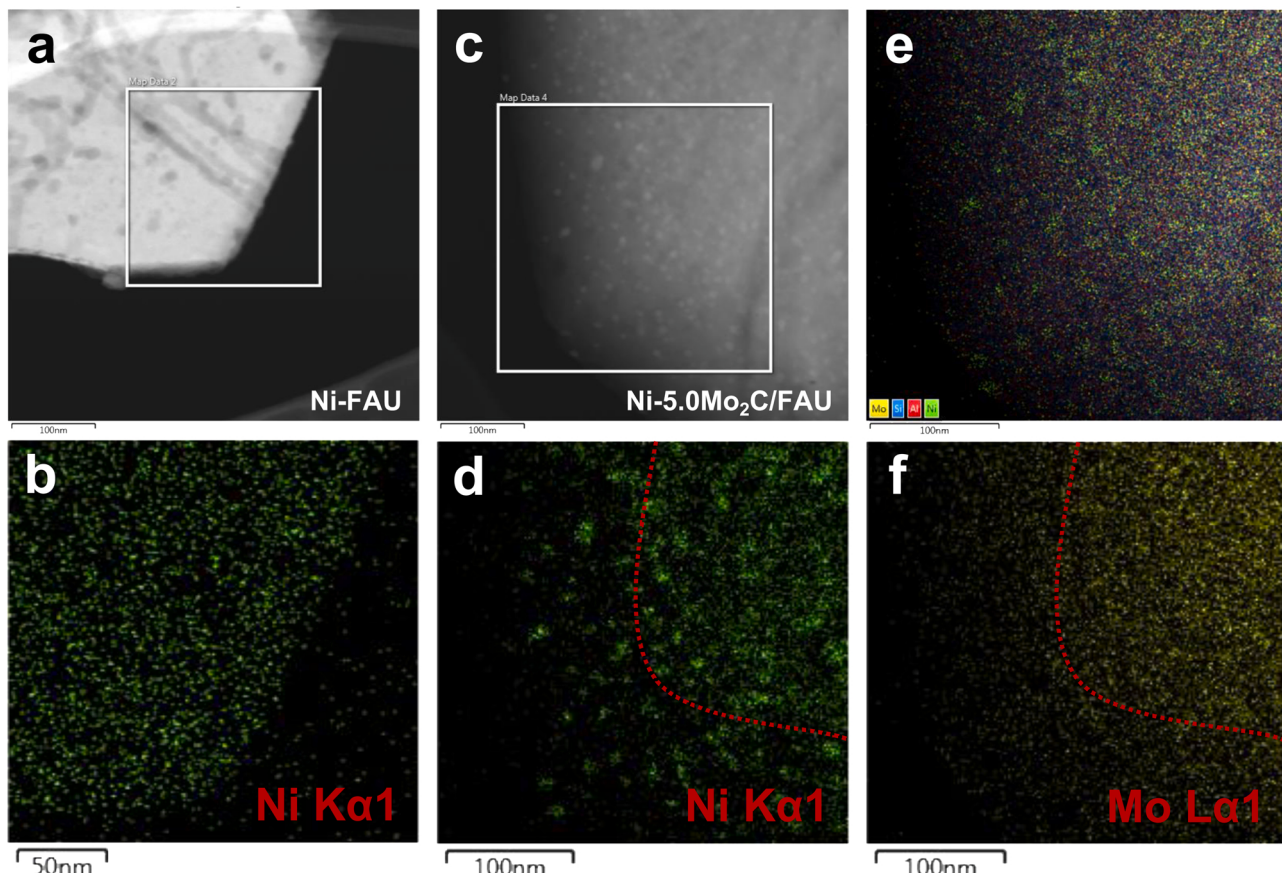


Fig. 3. HRTEM images of (a) Ni-FAU and (c) Ni-5.0Mo₂C/FAU, and the corresponding EDX elemental maps (the element type is labeled at the lower right corners) of Ni-FAU (b) and Ni-5.0Mo₂C/FAU (d-f).

particles is enhanced. Therefore, with higher Mo_2C loading, the dispersion of Ni on Ni-5.0 $\text{Mo}_2\text{C}/\text{FAU}$ (29.8%) is higher than on that of Ni-FAU, although heated for a much longer period.

In situ DRIFTS of CO adsorption experiments were conducted on Ni-FAU and Ni- $x\text{Mo}_2\text{C}/\text{FAU}$ to elucidate the electronic structure of Ni and the subtle impacts of Mo_2C loading (see Fig. 4). As the Mo loading increases, the intensity of adsorbed CO (2060 cm^{-1}) decreases gradually. The lowest intensity was recorded on Ni-1.0 $\text{Mo}_2\text{C}/\text{FAU}$, which presents nearly no evidence of adsorbed CO, while Ni-FAU presents the highest CO adsorption intensity. This indicates that the well-dispersed Mo_2C clusters likely modify the electron density of Ni^0 . Subsequently, for Ni- $x\text{Mo}_2\text{C}/\text{FAU}$ samples with $x \geq 1.5$, a new peak of adsorbed CO at a lower wavenumber of 2020 cm^{-1} , suggesting a stronger CO – site binding emerges. Its intensity increases as the Mo_2C loading or x increases. In addition, 5.0 $\text{Mo}_2\text{C}/\text{FAU}$ presents a peak with lower intensity at 2020 cm^{-1} , confirming this IR signal originates from the stretching vibration of CO adsorbed on Mo_2C particles. Indeed, these two IR peaks are attributed to CO adsorption at the Ni^0 sites (2060 cm^{-1}) and at the Mo_2C sites (2020 cm^{-1}). Surprisingly, the CO – Mo_2C binding dominants compared with CO adsorption at Ni^0 , strongly suggested by the absence of the peak at 2060 cm^{-1} for Ni- $x\text{Mo}_2\text{C}/\text{FAU}$ ($x = 1.5, 3.0, 5.0$ and 7.0) samples with high Mo_2C loading. It is also noticeable that only vibration of linear adsorbed CO ($2060 - 2019\text{ cm}^{-1}$) was detected, no vibration of the bridge-bonded CO ($1950 - 1750\text{ cm}^{-1}$) [33] was seen on Ni-FAU, which agrees with HRTEM-EDX data that Ni^0 is highly dispersed. The *in situ* DRIFTS on CO adsorption results suggest that the electronic structure of Ni within FAU has been impacted by the presence of Mo_2C , which leads to the change of its CO binding characteristic on the catalysts.

The catalytic performance of three samples, Ni-FAU, Ni-5.0 $\text{Mo}_2\text{C}/\text{FAU}$, and 5.0 $\text{Mo}_2\text{C}/\text{FAU}$, was evaluated using MSR reaction with the S/C ratio of 1.0 at $850\text{ }^\circ\text{C}$ for 27 h (see Fig. 5). Particularly, Ni-FAU has an initial CH_4 conversion of 35%, which decreases gradually as a function of time-on-stream until reaching 10% at the completion of the 27-hour test. The introduction of Mo_2C significantly increases both catalytic activity and stability. It is highlighted that the initial conversion of CH_4 , $\sim 70\%$, over Ni-5.0 $\text{Mo}_2\text{C}/\text{FAU}$, retains till the end of the 27-hour test. Interestingly, despite lower initial CH_4 conversion, H_2 yield, and CO yield of Ni-FAU compared with Ni-5.0 $\text{Mo}_2\text{C}/\text{FAU}$, the CO_2 yield of Ni-FAU is higher than that of Ni-5.0 $\text{Mo}_2\text{C}/\text{FAU}$. Such a phenomenon suggests the existence of a higher O/C ratio on the surface of Ni-FAU. We also noticed that $\text{Mo}_2\text{C}/\text{FAU}$ was not active in MSR (S/C ratio = 1.0) at $850\text{ }^\circ\text{C}$. Moreover, the influence of Mo loading on the same catalytic

MSR reaction using Ni- $x\text{Mo}_2\text{C}/\text{FAU}$ ($0.5 \leq x \leq 7.0$) was investigated (see Fig. S4 and Fig. S5). According to Fig. S4, at S/C = 1.0, Mo loading has a minor influence on the catalytic activity or stability. However, a significant effect of Mo loading on the performance is observed when the S/C ratio increases to 1.5 (see Fig. S5). According to Fig. S5, the initial activity of all Ni- $x\text{Mo}_2\text{C}/\text{FAU}$ samples appears to be independent of Mo loading, and presents an average CH_4 conversion of $\sim 70\%$. However, for Ni- $x\text{Mo}_2\text{C}/\text{FAU}$ with relatively low Mo loading of 0.5, 1.0 and 1.5 wt%, the CH_4 conversion decreases significantly to 5% after 25 h on stream. At $x = 3.0$, the final CH_4 conversion following the 25-hour test is $\sim 35\%$. Notably, further increase in Mo loading to 5.0 and 7.0 wt% leads to stable MSR catalyst under the reaction condition with nearly no deactivation throughout the length of tests. Hence, our Mo loading test strongly suggests the enhanced stability for Ni- $x\text{Mo}_2\text{C}/\text{FAU}$ with higher Mo_2C loading in the MSR reaction when the S/C ratio of 1.5 was used.

The activation energies (E_a) were estimated and compared in the kinetic region (see Fig. 6). The Arrhenius plots of all Ni- $x\text{Mo}_2\text{C}/\text{FAU}$ samples at S/C ratios of 1.0 and 1.5 are in Fig. S8. Specifically, the E_a is determined to be $158 \pm 5\text{ kJ/mol}$ in MSR catalyzed by Ni-FAU at S/C = 1.0 (Fig. 6a). However, at S/C = 1.5, E_a cannot be calculated because of the low stability of Ni-FAU catalyst under the given MSR reaction condition. As Mo content increases, the magnitude of E_a systematically evolves (Fig. 6b). At S/C = 1.0, all Ni- $x\text{Mo}_2\text{C}/\text{FAU}$ catalysts share similar E_a , approximately 75.0 kJ/mol, and the Mo loading appears not to impact the magnitude of E_a . Interestingly, at S/C = 1.5, the E_a magnitude decreases from 117 kJ/mol to 77.0 kJ/mol as the Mo loading increases from 0.5 to 3.0 wt%. It appears that further increasing the Mo loading beyond 3.0 wt% has no significant effect on the activation energy. Overall, the evolution of E_a as a function of Mo loading and S/C is consistent with the catalytic performance results.

The post-stability-test or spent (spt-) samples were examined by XRD and TEM for phase and morphological evaluations, respectively (see Fig. 7, Fig. S6, and Fig. S9). Generally, Fig. 1 and Fig. 7 suggest that all samples retain the cubic FAU ($Fd\bar{3}m$) structure of zeolite Y except spt-5.0 $\text{Mo}_2\text{C}/\text{FAU}$, which shows detectable evidence of framework degradation. For comparison and interpretation, we combined the XRD data of fresh Ni- $x\text{Mo}_2\text{C}/\text{FAU}$ and spt-Ni- $x\text{Mo}_2\text{C}/\text{FAU}$ samples with Mo loading of 3.0, 5.0, and 7.0 wt% in Fig. S9. Interestingly, a new diffraction peak emerges at 39.5 ° on the spent samples with Mo loading higher than 3.0 wt% (see Fig. S9). This peak belongs to the (121) reflection of Mo_2C , which is likely to be a product of sintering and crystallization of the amorphous Mo_2C particles under harsh MSR reaction condition. Similar phenomena were also observed in multiple

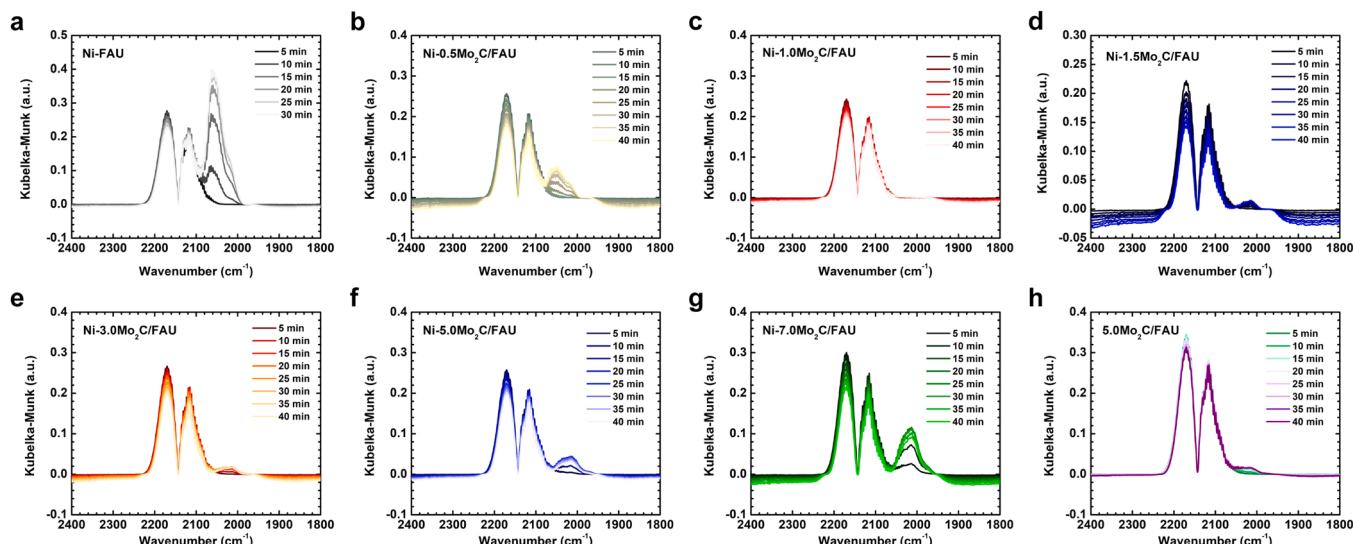


Fig. 4. *In situ* CO adsorption DRIFTS results on all fresh catalyst samples at room temperature.

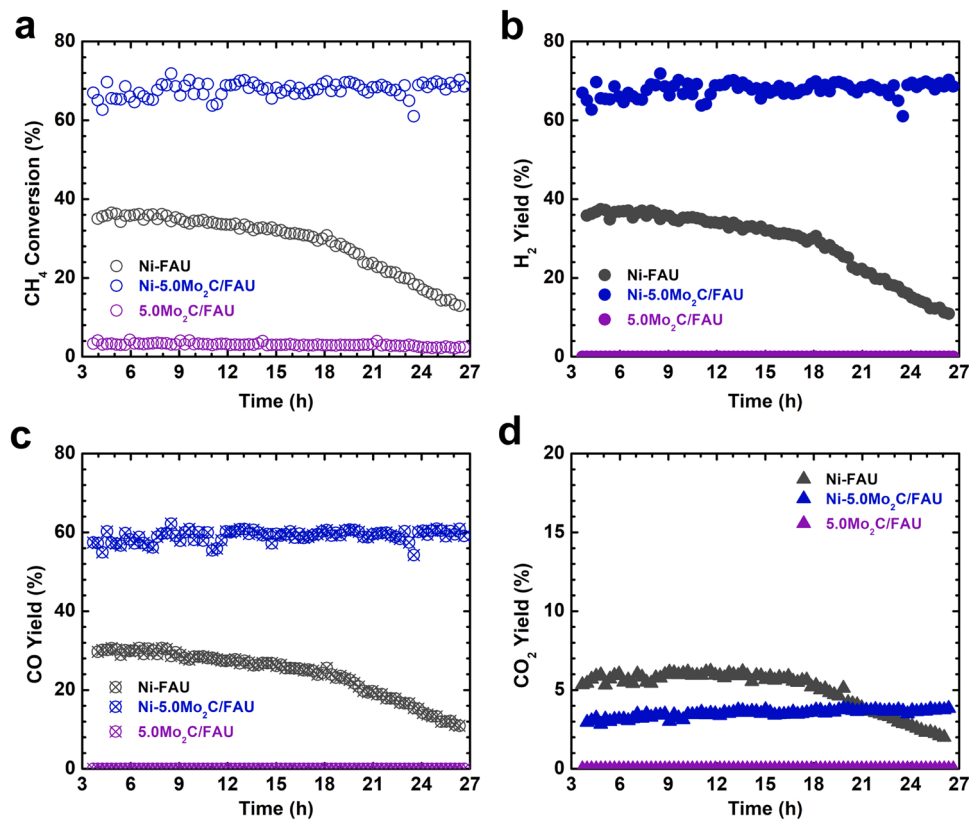


Fig. 5. Performance test of Ni-FAU, Ni-5.0Mo₂C/FAU and 5.0Mo₂C/FAU in MSR at 850 °C with 55 mg of catalyst, F_{methane} = 20.3 sccm, S/C = 1.0, and bed height of 0.4 cm.

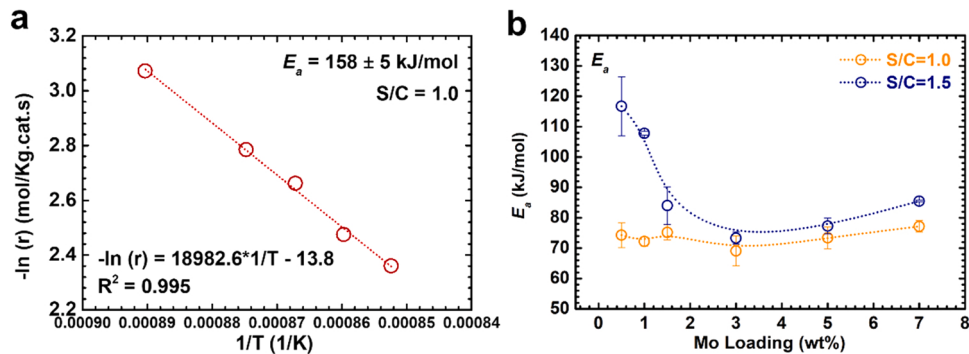


Fig. 6. (a) The Arrhenius plot of MSR reaction (S/C = 1.0) on Ni-FAU, and (b) E_a values of Ni-xMo₂C/FAU (0.5 ≤ x ≤ 7.0) where "x" is the Mo wt%. The MSR reactions were performed on 25 mg of catalyst at 850 °C with F_{methane} = 20.3 sccm, S/C = 1.0 and 1.5, F_{nitrogen} = 10 sccm and bed height of 0.2 cm.

studies on supported Mo species, by Joshua *et. al.* on MoP at above 600 °C, and by Okuyama *et. al.* in growing Mo₂C particles from its amorphous phase via ion bombardment. [34,35] The TEM images shown in Fig. S6 elucidate that sintering is a shared phenomenon for all samples. More specifically, Ni NPs (~100 nm) were observed on the external surface of *spt*-Ni-FAU. On all *spt*-Ni-xMo₂C/FAU samples, the particle size increases and distribution widens compared with corresponding fresh Ni-xMo₂C/FAU. However, these particles tend to be smaller than Ni particles on *spt*-Ni-FAU. In addition, the amount of carbon or coke increases as the Mo loading increases. Fig. S6 shows that below 3.0 wt%, no filament carbon is detected, while it increasingly builds up as the Mo content increases to 7.0 wt%. This observation suggests that the Mo₂C in *spt*-Ni-xMo₂C/FAU promotes CH₄ activation. We also noticed that there appears to be no filament carbon on *spt*-5.0Mo₂C/FAU (i.e., the sample without Ni).

The *spt*-Ni-FAU and Ni-5.0Mo₂C/FAU were also characterized by

HRTEM (Fig. 8a) and EDX (Fig. 8b) to elucidate any potential changes of Ni and Mo₂C dispersion after MSR reaction (The signals of Si and Al are in Fig. S7). In Figs. 8a and 8b, on *spt*-Ni-FAU, Ni particles around 125 nm were observed, a strong indication of severe sintering of Ni particles on FAU support without the presence of Mo₂C. For the *spt*-Ni-5.0Mo₂C/FAU sample (Fig. 8c-f), its HRTEM images and EDX mappings suggest that Mo₂C remains highly dispersed on FAU support after MSR reaction at 850 °C for 24 h. Although sintering was also observed for Ni on Ni-5.0Mo₂C/FAU, the particle size of Ni only grew to 8.3 nm after the MSR reaction, which could be ascribed to the presence of Mo₂C.

To quantify the coke formation and coking site distribution, TPO experiments using integrated TG-DSC-MS were performed on each spent sample (see Fig. 9). TPO results suggest that thermal oxidation of spent samples is stepwise with two major stages. In *Stage I*, TG curve levels at temperature below 300 °C, which is primarily owing to endothermic dehydration evidenced by DSC and MS curves (*m/z* = 18, see Fig. 9b and

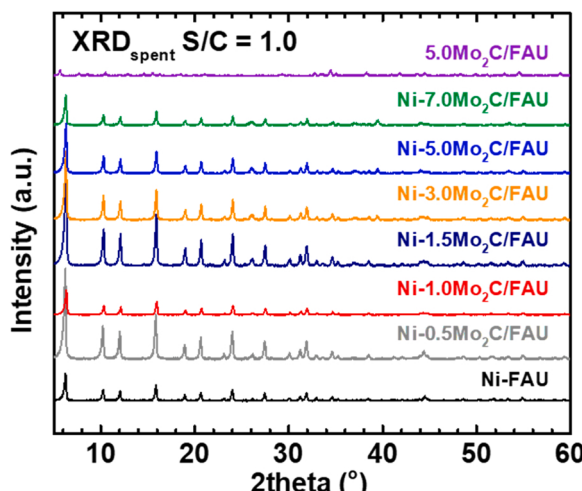


Fig. 7. Ex situ XRD patterns at room temperature of all spent catalyst samples after MSR at 850 °C with 55 mg of catalyst, $F_{\text{methane}} = 20.3 \text{ sccm}$, S/C = 1.0, and bed height of 0.4 cm.

c). Within *Stage I*, no detectable CO_2 signal was recorded by MS (Fig. 9d). In *Stage II*, the combustion of coke (carbon) in oxidative atmosphere starts at about 400 °C, which leads to significantly exothermic DSC peaks due to combustion spanning from ~ 400–700 °C (see Fig. 9b and d). In this process, CO_2 ($m/z = 44$) is released. Based on the amount of CO_2 generated, we can quantify the coke on each spent sample.

According to Fig. 9, the *spt*-Ni-FAU sample shows a negligible amount of coking. The general trend for all $\text{Ni}-x\text{Mo}_2\text{C}/\text{FAU}$ samples is that as the Mo content increases, the degree of coking increases: the amount of coke increases from 0.4% to 4.4 wt% as the Mo loading increases from 0.0 to 7.0 wt%, respectively. Moreover, at Mo loading higher than 3.0, we were able to distinguish the “light coke” (C_L) centered at about 540 °C, and the “hard coke” (C_H) peaked at about 610 °C (see Fig. S10). Particularly, the $\text{C}_L:\text{C}_H$ ratio is approximately 1:2 for $\text{Ni}-3.0\text{Mo}_2\text{C}/\text{FAU}$, 2:1 for $\text{Ni}-5.0\text{Mo}_2\text{C}/\text{FAU}$, and 3:1 for $\text{Ni}-7.0\text{Mo}_2\text{C}/\text{FAU}$. The $\text{C}_L:\text{C}_H$ ratio of $5.0\text{Mo}_2\text{C}/\text{FAU}$ is ~ 3.5:1. Such distribution suggests at least two types of coke exist. Specifically, C_L , which has the highest ratio on *spt*- $5.0\text{Mo}_2\text{C}/\text{FAU}$, was from amorphous coke and was formed around Mo_2C that is not in contact with Ni (see Fig. S6). In contrast, C_H , the filament carbon, was generated potentially at the $\text{Mo}_2\text{C}-\text{Ni}$ active sites considering it is mainly formed on *spt*- $\text{Ni}-x\text{Mo}_2\text{C}/\text{FAU}$ samples. Therefore, consistent results from TEM and thermal analysis confirm that the presence of Mo_2C promotes CH_4 activation in MSR reaction on $\text{Ni}-x\text{Mo}_2\text{C}/\text{FAU}$, evidenced by the increased degree of coke formation as more Mo_2C is introduced.

3.1. Ni-FAU deactivation Mechanisms

To further elucidate the deactivation mechanism of Ni-FAU, first we examined the MSR performance of Ni-FAU at 850 °C at S/C = 1.0 and 1.5 (see Fig. 10a-d). Typically, the two catalytic deactivation mechanisms in MSR, (i) coking and (ii) sintering, respond differently as a function of the S/C ratio. Once coking dominants, a higher S/C ratio results in higher catalytic stability owing to promoted oxidation rate.

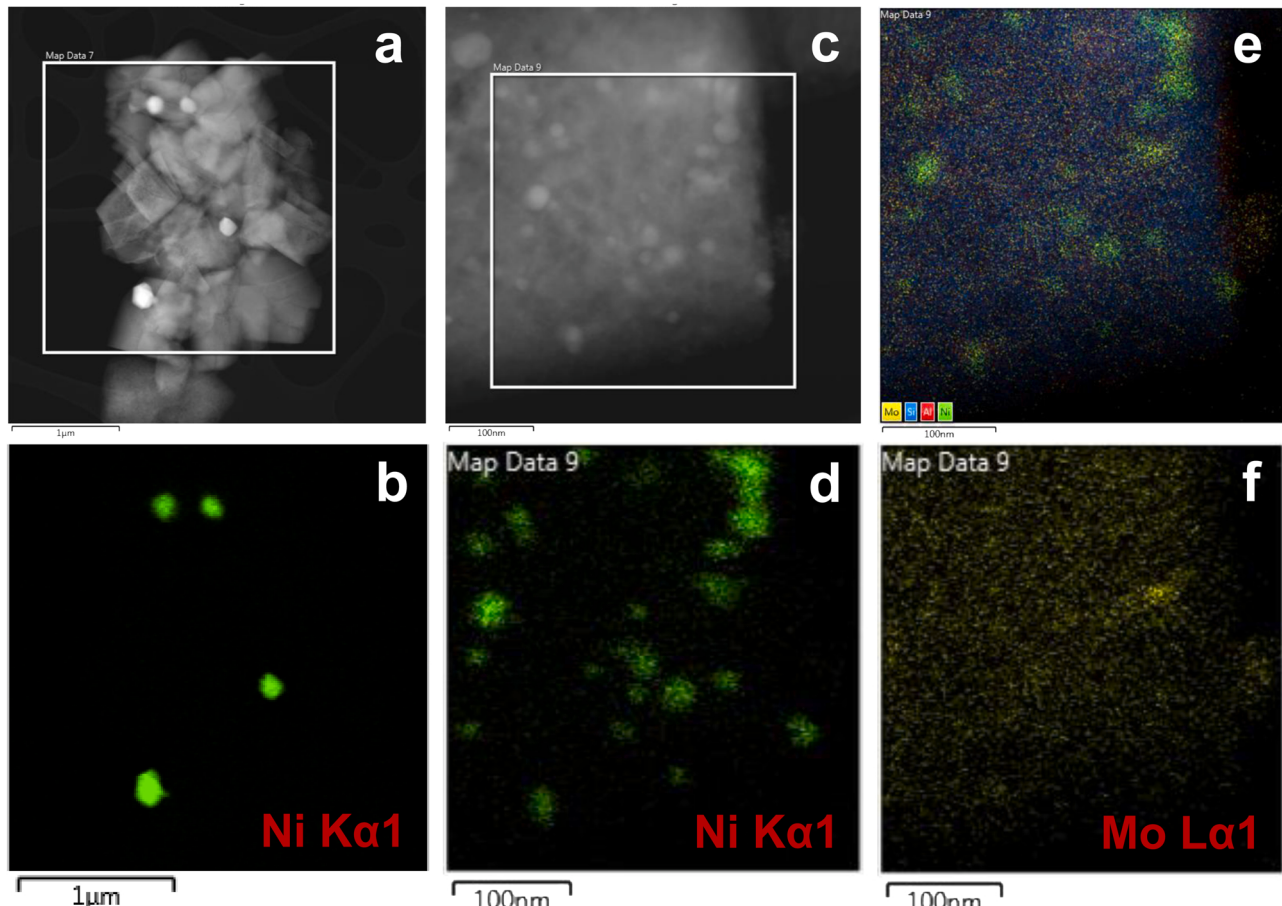


Fig. 8. HRTEM images (a) *spt*-Ni-FAU and (c) *spt*-Ni-5.0Mo₂C/FAU and the corresponding EDX elemental maps (the element type is labeled at the lower right corners) of *spt*-Ni-FAU (b) and *spt*-Ni-5.0Mo₂C/FAU (d-f).

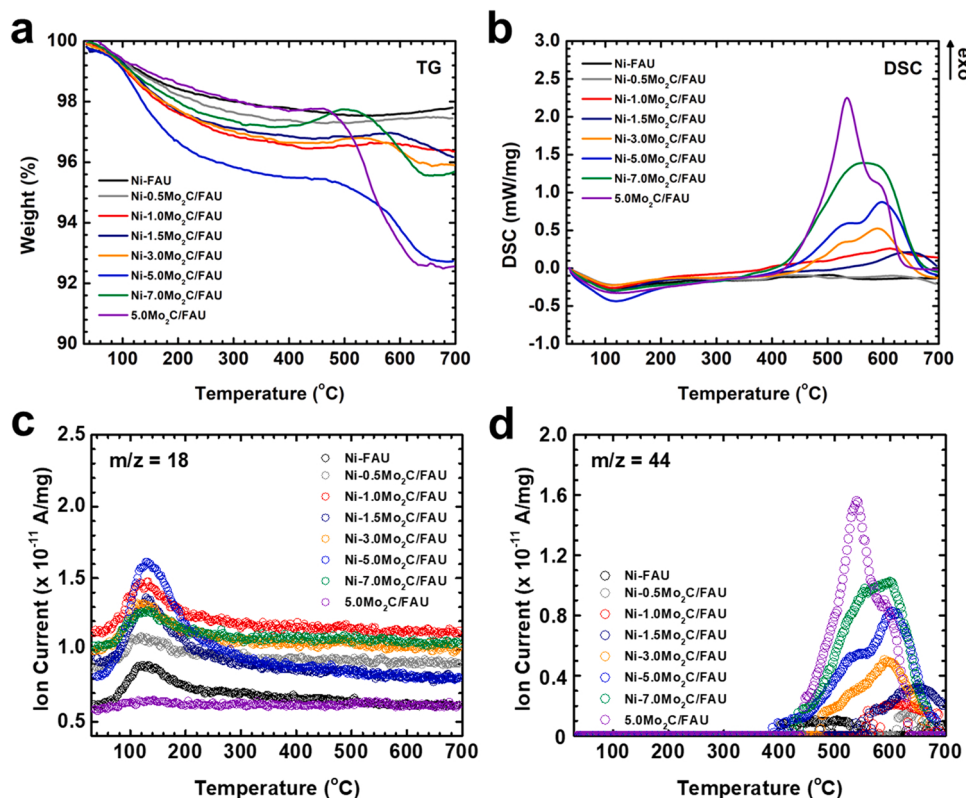


Fig. 9. TPO results of all spent catalyst samples after MSR on 55 mg of catalysts at 850 °C with $F_{\text{methane}} = 20.3 \text{ sccm}$, $S/C = 1.0$, and bed height of 0.4 cm. (a) TG, (b) DSC, (c) MS of H_2O ($m/z = 18$), and (d) MS of CO_2 ($m/z = 44$). These TPO experiments were carried out using an integrated TG-DSC-MS system in the temperature range of 30–700 °C (10 °C/min) under O_2 flow (10 vol% O_2 , 60 mL/min).

When sintering is responsible for the deactivation, the S/C ratio increase leads to decreased catalytic stability due to higher surface OH group concentration, at which particle sintering is favorable. Our experimental observation is that the stability of Ni-FAU at $S/C = 1.5$ significantly

decreases from 65% to ~10% within 90 min (Fig. 10a-b). Most existing reports suggest although higher S/C inhibit coking, the presence of steam promotes sintering of Ni NPs in MSR, resulting in catalyst deactivation. For example, Bartholomew *et. al.* reviewed the sintering

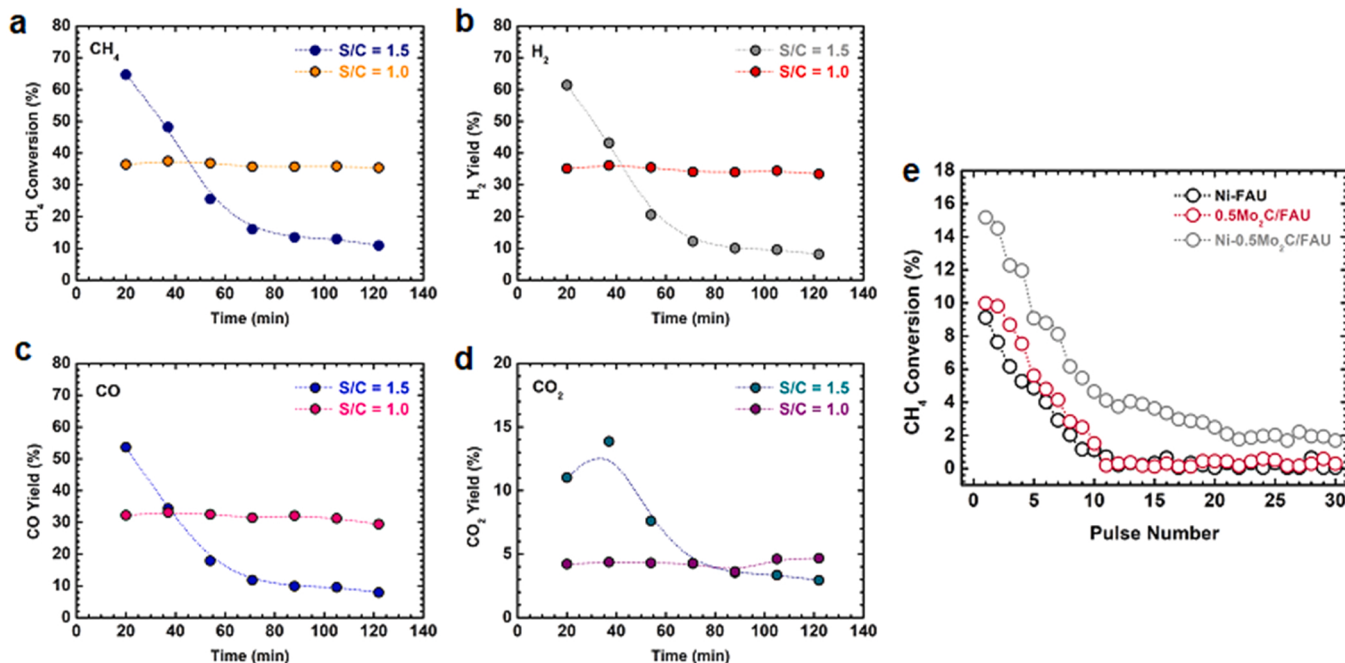


Fig. 10. Performance test of Ni-FAU in MSR at 850 °C with $S/C = 1.0$ and 1.5. (a) CH_4 conversion, (b) H_2 yield, (c) CO yield, and (d) CO_2 yield. The MSR reaction tests were performed on 55 mg of catalyst at 850 °C with $F_{\text{methane}} = 20.3 \text{ sccm}$, $S/C = 1.0$ and 1.5, and bed height of 0.4 cm. (e) CH_4 conversion results of methane pulse reaction over Ni-FAU, Ni-0.5Mo₂C/FAU, and 0.5Mo₂C/FAU samples at 850 °C.

kinetics of Ni in pure H₂ and 3%H₂O (steam)/H₂ atmosphere at temperatures ranging from 630 to 830 °C. [36] They pointed out that at a given temperature, in steam, the rate of Ni NP sintering was significantly higher compared with the rate under dry conditions. By coupling experimental reaction kinetic with DFT computational methods, Sehested *et. al.* reported that above 700 °C the sintering rate of Ni NPs deviated from the particle migration and coalescence models, yet their data fit Ostwald ripening well. [37] They further proposed that the Ni₂-OH clusters, which have a diffusion rate 700 times higher than that of Ni atoms, were likely responsible for the quick sintering of Ni in MSR.

The stability of supported metal catalysts is closely related to the competing metal-metal interparticle interactions and the metal-support binding. Once the metal – support bonds are robust, it is typically considered that the supported metal particles are highly dispersed leading to increased activity with improved resistance to sintering. Ostwald ripening, a thermodynamically governed particle growth phenomenon involving interparticle interactions, is traditionally less employed by the catalysis community to explain the growth of supported catalytic particles and catalyst deactivation. To harness Ostwald ripening for MSR catalytic system, the formation of hydroxylated Ni surface has to be favored. Recently, Li *et. al.* studied the coke formation on Ni/ZrO₂ as a function of Ni content. [38] It was found that both reforming activity and coking rate decreased as the Ni loading decreased. In other words, catalysts with low Ni loading and high dispersion are supposed to have low MSR activity. Furthermore, Xu *et. al.* and Cui *et. al.* also investigated the rate of CH₄ decomposition on Ni/Al₂O₃ with different Ni particle sizes, achieved by altering Ni loading. [39,40] It was found that between 7.0 and 39.7 nm the initial turnover frequency (TOF) increased as a function of Ni particle size, and the maximum TOF was obtained when the average size of Ni NPs is 31.8 nm. In this study, TEM and EDX images of the Ni-FAU samples (Fig. 3 and S3) demonstrate that the size of Ni clusters is too small to be precisely measured. With such a small Ni particle size, the CH₄ decomposition rate on Ni-FAU would be considerably low. Such low CH₄ activity of Ni-FAU is responsible for promoting the formation of the hydroxylated Ni surface (i.e., the reaction between H₂O and Ni surface), which leads to severe sintering via Ostwald ripening. Both the TEM images and TPO results are in excellent agreement with this sintering-based deactivation mechanism of Ni-FAU in MSR where a significant particle size growth of Ni (~100 nm) and the absence of coking coexist. The Ni particles with significantly increased size and hydroxylated surface are responsible for the poor stability of Ni-FAU in MSR operating at S/C = 1 and 850 °C. In order to enhance its stability, one needs to increase its CH₄ activity and balance the H₂O oxidation reaction. Our study is a well-defined example demonstrating the mechanism of metallic catalyst particle growth through Ostwald ripening under the presence of water.

3.2. Roles of Mo₂C particles in MSR on Ni-xMo₂C/FAU

The introduction of Mo₂C (5.0 wt%) to Ni-FAU significantly decreases its E_a to 75.0 kJ/mol for Ni-5.0Mo₂C/FAU in MSR, compared with that of Ni-FAU (158 kJ/mol) as shown in Fig. 6. Consequently, their catalytic activity and stability in MSR are enhanced (Fig. 5). In Figs. S6 and 9, the TEM images and TPO results suggest a higher degree of coking on spt-Ni-5.0Mo₂C/FAU (3.4 wt%) compared with that on spt-Ni-FAU (0.4 wt%). We notice that in TPO, the coke formed on spt-5.0Mo₂C/FAU (4.6 wt%) is even higher than that of spt-Ni-5.0Mo₂C/FAU sample (see Fig. 9). However, without Ni pre-loaded, 5.0Mo₂C/FAU is not active in MSR at 850 °C with no products, such as H₂ and CO, detected. These experimental data suggest that (i) the CH₄ activation rate on Mo₂C is faster than the carbon consumption (i.e., the H₂O reaction with the carbon) rate in MSR operating at S/C = 1.0 and 850 °C, and (ii) the Mo₂C NP itself on 5.0Mo₂C/FAU is MSR-inactive due to coking caused by its faster CH₄ activation rate than the carbon consumption rate.

For quantitative confirmation of CH₄ activation increase after the introduction of Mo₂C on Ni-FAU, we carried out CH₄ pulse reaction at 850 °C on Ni-FAU, Ni-0.5Mo₂C/FAU, and 0.5Mo₂C/FAU samples (see Fig. 10e). The initial conversions of CH₄ over Ni-FAU, Ni-0.5Mo₂C/FAU, and 0.5Mo₂C/FAU samples are 9%, 15%, and 10%, respectively. This provides further confirmation that the significant increase in the CH₄ activation rate observed here is tightly related to Mo₂C loading to Ni catalyst. The CH₄ conversions over Ni-FAU and 0.5Mo₂C/FAU are quite similar. However, considering Ni_(Ni-FAU): Mo_(0.5Mo₂C/FAU) = ~ 4:1 (i.e., 4 times more weight of Ni was used for Ni-FAU than Mo used for 0.5Mo₂C/FAU), the mass-based CH₄ activation activity on 0.5Mo₂C/FAU is indeed approximately 4 times higher than that of Ni-FAU. Hence, the CH₄ pulse test results further assure that Mo₂C introduction significantly promotes the CH₄ decomposition rate of Ni-xMo₂C/FAU catalysts. For MSR operating at S/C = 1 and 850 °C, the sufficient amount of Mo₂C presented in Ni-xMo₂C/FAU catalysts can prevent the Ni hydroxylation and Ni sintering by promoting the carbon formation from the enhanced CH₄ activation rate. In other words, as the rate of carbon formation increases, H₂O reacts with these carbons instead of the Ni surface, which inhibits the Ni surface oxidation.

The role of Mo₂C was further studied with MSR reaction by investigating the effect of Mo loading on the MSR performance at S/C = 1 and 850 °C. According to Fig. S4, the Mo₂C loading on Ni-xMo₂C/FAU samples has nearly no influence in MSR, and the conversion of CH₄ is in a narrow range, between 65% and 70%, with E_a = 75.0 kJ/mol. Meanwhile, the TPO results of spent samples show increased coke formation as more Mo is added. Especially, the TEM image of spt-Ni-7.0Mo₂C/FAU (Fig. S6) shows that the particles are decorated/coated by the carbon filament. This suggests that the rate of carbon formation is faster than the carbon consumption rate for Ni-xMo₂C/FAU samples with the high Mo loading (e.g., 7 wt% Mo) in MSR operating at S/C = 1.0 and 850 °C. In such a case, one needs to increase the H₂O activity to balance the rates of carbon formation and carbon consumption.

In order to increase the H₂O activity, we carried out MSR reactions on Ni-xMo₂C/FAU samples at S/C ratio = 1.5 and 850 °C (Fig. S5). We noticed that in the 25-hour test, only Ni-5.0Mo₂C/FAU and Ni-7.0Mo₂C/FAU retained their high activity, while for samples with Mo lower than 5.0 wt%, the activity gradually decreased. We also noticed that the amount of coke on spt-Ni-xMo₂C/FAU increases from 0.7 to 2.8 wt% as the Mo loading increases from 1.5 to 7.0 wt% (Fig. S11). Thus, at Mo loading of 1.5 and 3.0 wt%, only a small amount of coke was detected on the spent samples. For Ni-xMo₂C/FAU with insufficient Mo₂C (e.g., Mo loading less than 5.0 wt%), their MSR performance and TPO data indicate that the CH₄ activation rate is inadequate to balance the H₂O. As a result, they show significant deactivations in MRS operating at S/C ratio = 1.5 and 850 °C (Fig. S5) by promoting the surface Ni oxidation and sintering. On the other hand, Ni-5.0Mo₂C/FAU and Ni-7.0Mo₂C/FAU samples possess a sufficient amount of Mo₂C to promote adequate CH₄ activity for balancing H₂O. Hence, their stability increases significantly in MRS operating at S/C ratio = 1.5 and 850 °C by increasing CH₄ activation rate.

3.3. The structures of active sites on Ni-xMo₂C/FAU

Direct experimental results suggest that the active sites on Ni-xMo₂C/FAU are Mo₂C decorated Ni particles. Moreover, multiple pieces of evidence strongly support that the role of Mo₂C is to decompose CH₄ while the Ni particles activate H₂O. *First*, the EDX elemental mappings of the fresh Ni-5.0Mo₂C/FAU suggest that both Ni and Mo₂C are highly dispersed with significantly overlapped ranges of distribution. For spt-Ni-5.0Mo₂C/FAU, Mo₂C remains well-dispersed and the distributions of Ni and Mo₂C are still overlapped. Moreover, the *in situ* CO adsorption DRIFTS data strongly suggest that the electronic structure of the Ni NPs has been perturbed by Mo₂C (see Fig. 4). Hence, it is clear that the introduction of Mo₂C improves the activity and stability of Ni-FAU in MSR reaction by boosting the CH₄ activation rate at the vicinity of Ni

sites. *Secondly*, the catalytic performance results highlight that, without co-existed metallic Ni, 5.0Mo₂C/FAU sample presents no MSR activity (see Fig. 5). Meanwhile, severe coking is detected on the *spt*-5.0Mo₂C/FAU in the TPO experiments instead of sintering, leading to near-zero MSR activity. Interestingly, the amount of coke on *spt*-5.0Mo₂C/FAU was quantified to be ~4.6 wt%, which is much higher than that on the *spt*-Ni-5.0Mo₂C/FAU (~3.4 wt%). In contrast, the sample without Mo₂C, Ni-FAU, exhibits much lower activity and lower stability because of sintering. This suggests that the enhanced MSR performance observed on Ni-*x*Mo₂C/FAU originates from the interplays between Ni and Mo₂C particles and is not solely due to CH₄ activation on the Mo₂C. *Thirdly*, two types of coke are found on the *spt*-Ni-*x*Mo₂C/FAU. The filament carbon, “hard coke”, is common on *spt*-Ni-*x*Mo₂C/FAU samples, but not on *spt*-Ni-FAU and *spt*-5.0Mo₂C/FAU, reflecting the formation of the new active sites, Mo₂C-Ni, on Ni-*x*Mo₂C/FAU samples. These sites are where the MSR occurs and are responsible for (i) the formation of filament carbon on the catalyst samples with high Mo₂C loadings at the S/C ratio of 1.0, and (ii) the better catalytic stability at the S/C ratio of 1.5.

4. Conclusions

In this study, we designed and synthesized a family of catalysts with tuned Ni and Mo₂C supported on zeolite Y (FAU) for gas-phase catalytic MSR at 850 °C. After systematic material characterizations, MSR performance tests, and reaction kinetics studies, we successfully elucidated the (i) deactivation mechanism of Ni sites, (ii) the promoting role of Mo₂C on both catalytic activity and stability. First of all, the deactivation of metallic Ni sites features a highly dynamic mechanism with two competing factors, namely, Ni particle sintering and CH₄ activation at the Ni sites. Because of its low activity towards CH₄ in MSR, the surface of Ni particles is hydroxylated, which results in energetically favorable particle affinity resulting in fast sintering. We also point out that Mo₂C promotes MSR reaction by taking advantage of its strong activity toward the CH₄ activation, evidenced by the positively correlated Mo loadings and degree of coking. The analysis of coke types further indicates that the active sites for MSR are Mo₂C-Ni on Ni-*x*Mo₂C/FAU samples, not pure Mo₂C which is too active in methane decomposition. Thus, integration of Ni and Mo₂C on FAU enhances CH₄ activation, inhibits Ni hydroxylation, and balances the rates of carbon formation and consumption, which enables increased catalyst stability.

CRediT authorship contribution statement

Xianghui Zhang: Conceptualization, Methodology, Validation, Formal analysis, Investigation, Writing – original draft, Writing – review & editing, Visualization. **Kyungmin Yim:** Formal analysis, Visualization. **Jinsoo Kim:** Formal analysis, Visualization. **Di Wu:** Conceptualization, Methodology, Investigation, Resources, Writing – review & editing, Visualization, Supervision, Project administration. **Su Ha:** Conceptualization, Methodology, Investigation, Resources, Writing – review & editing, Supervision, Project administration.

Declaration of Competing Interest

The authors declare that they have no known competing financial interests or personal relationships that could have appeared to influence the work reported in this paper.

Acknowledgement

This work was supported by institutional funds from the Gene and Linda Voiland School of Chemical Engineering and Bioengineering, O.H. Reaugh Laboratory for Oil and Gas Research, and Alexandra Navrotsky Institute for Experimental Thermodynamics at Washington State University. Xianghui Zhang is supported by the Chambroad Distinguished Scholarship at Washington State University.

Appendix A. Supporting information

Supplementary data associated with this article can be found in the online version at doi:10.1016/j.apcatb.2022.121250.

References

- M. Momirlan, T.N. Veziroglu, Current status of hydrogen energy, *Renew. Sustain. Energy Rev.* 6 (2002) 141–179, [https://doi.org/10.1016/S1364-0321\(02\)00004-7](https://doi.org/10.1016/S1364-0321(02)00004-7).
- P.P. Edwards, V.L. Kuznetsov, W.I. David, Hydrogen energy, *Philos. Trans. R. Soc. A Math. Phys. Eng. Sci.* 365 (2007) 1043–1056, <https://doi.org/10.1098/rsta.2006.1965>.
- B. Tanç, H.T. Arat, E. Baltacıoğlu, K. Aydin, Overview of the next quarter century vision of hydrogen fuel cell electric vehicles, *Int. J. Hydrog. Energy* 44 (2019) 10120–10128, <https://doi.org/10.1016/j.ijhydene.2018.10.112>.
- E.L.V. Eriksson, E.M.A. Gray, Optimization and integration of hybrid renewable energy hydrogen fuel cell energy systems – a critical review, *Appl. Energy* 202 (2017) 348–364, <https://doi.org/10.1016/j.apenergy.2017.03.132>.
- E.S. Hanley, J.P. Deane, B.P.O. Gallachóir, The role of hydrogen in low carbon energy futures—a review of existing perspectives, *Renew. Sustain. Energy Rev.* 82 (2018) 3027–3045, <https://doi.org/10.1016/j.rser.2017.10.034>.
- E. Meloni, M. Martino, A short review on Ni based catalysts and related engineering issues for methane steam reforming, *Catalysts* 10 (2020) 352, <https://doi.org/10.3390/catal10030352>.
- Z. Wang, X.M. Cao, J. Zhu, P. Hu, Activity and coke formation of nickel and nickel carbide in dry reforming: a deactivation scheme from density functional theory, *J. Catal.* 311 (2014) 469–480, <https://doi.org/10.1016/j.jcat.2013.12.015>.
- D.L. Trimm, Coke formation and minimisation during steam reforming reactions, *Catal. Today* 37 (1997) 233–238, [https://doi.org/10.1016/S0920-5861\(97\)00014-X](https://doi.org/10.1016/S0920-5861(97)00014-X).
- K.O. Christensen, D. Chen, R. Lødeng, A. Holmen, Effect of supports and Ni crystal size on carbon formation and sintering during steam methane reforming, *Appl. Catal. A Gen.* 314 (2006) 9–22, <https://doi.org/10.1016/j.apcata.2006.07.028>.
- C.J. Liu, J. Ye, J. Jiang, Y. Pan, Progresses in the preparation of coke resistant Ni-based catalyst for steam and CO₂ reforming of methane, *ChemCatChem* 3 (2011) 529–541, <https://doi.org/10.1002/cctc.201000358>.
- Y. Zhang, W. Wang, Z. Wang, X. Zhou, Z. Wang, C.-J. Liu, Steam reforming of methane over Ni/SiO₂ catalyst with enhanced coke resistance at low steam to methane ratio, *Catal. Today* 256 (2015) 130–136, <https://doi.org/10.1016/j.cattod.2015.01.016>.
- M.A. Nieva, M.M. Villaverde, A. Monzón, T.F. Garetto, A.J. Marchi, Steam-methane reforming at low temperature on nickel-based catalysts, *Chem. Eng. J.* 235 (2014) 158–166, <https://doi.org/10.1016/j.cej.2013.09.030>.
- A.C.S.C. Teixeira, R. Giudici, Deactivation of steam reforming catalysts by sintering: experiments and simulation, *Chem. Eng. Sci.* 54 (1999) 3609–3618, [https://doi.org/10.1016/S0009-2509\(98\)00516-8](https://doi.org/10.1016/S0009-2509(98)00516-8).
- C.H. Bartholomew, Sintering kinetics of supported metals: new perspectives from a unifying GPLE treatment, *Appl. Catal. A, Gen.* 107 (1993) 1–57, [https://doi.org/10.1016/0926-860X\(93\)85114-5](https://doi.org/10.1016/0926-860X(93)85114-5).
- T.W. Hansen, A.T. Delariva, S.R. Challa, A.K. Datye, Sintering of catalytic nanoparticles: particle migration or owsald ripening? *Acc. Chem. Res.* 46 (2013) 1720–1730, <https://doi.org/10.1021/ar3002427>.
- J. Sehested, A. Carlsson, T.V.W. Janssens, P.L. Hansen, A.K. Datye, Sintering of nickel steam-reforming catalysts on MgAl₂O₄ spinel supports, *J. Catal.* 197 (2001) 200–209, <https://doi.org/10.1006/jcat.2000.3085>.
- M. Boudjeloud, A. Boulahouache, C. Rabia, N. Salhi, La-doped supported Ni catalysts for steam reforming of methane, *Int. J. Hydrog. Energy* 44 (2019) 9906–9913, <https://doi.org/10.1016/j.ijhydene.2019.01.140>.
- K. Lertwittayanan, W. Youravong, W. Jye, Enhanced catalytic performance of Ni/α-Al₂O₃ catalyst modified with CaZrO₃ nanoparticles in steam-methane reforming, *Int. J. Hydrog. Energy* 42 (2017) 28254–28265, <https://doi.org/10.1016/j.ijhydene.2017.09.030>.
- F. Morales-cano, L.F. Lundsgaard, R.R. Tiruvalam, H. Falsig, M.S. Skjøth-rasmussen, Improving the sintering resistance of Ni/Al₂O₃ steam-reforming catalysts by promotion with noble metals, *Appl. Catal. A Gen.* 498 (2015) 117–125, <https://doi.org/10.1016/j.apcata.2015.03.016>.
- D. Pashchenko, Experimental investigation of reforming and flow characteristics of a steam methane reformer filled with nickel catalyst of various shapes, *Energy Convers. Manag.* 185 (2019) 465–472, <https://doi.org/10.1016/j.enconman.2019.01.103>.
- E. Environ, Z. Chen, D. Higgins, A. Yu, J. Zhang, A review on non-precious metal electrocatalysts for PEM fuel cells, *Energy Environ. Sci.* 4 (2011) 3167–3192, <https://doi.org/10.1039/c0ee00558d>.
- P.K. Cheekatamarla, C.M. Finnerty, Reforming catalysts for hydrogen generation in fuel cell applications, *J. Power Sources* 160 (2006) 490–499, <https://doi.org/10.1016/j.jpowsour.2006.04.078>.
- Y. Ma, G. Guan, X. Hao, J. Cao, A. Abudula, Molybdenum carbide as alternative catalyst for hydrogen production – a review, *Renew. Sustain. Energy Rev.* 75 (2017) 1101–1129, <https://doi.org/10.1016/j.rser.2016.11.092>.
- T.L. Levalley, A.R. Richard, M. Fan, The progress in water gas shift and steam reforming hydrogen production technologies - a review, *Int. J. Hydrog. Energy* 39 (2014) 16983–17000, <https://doi.org/10.1016/j.ijhydene.2014.08.041>.
- K.D. Sabinis, Y. Cui, M.C. Akatay, M. Shekhar, W. Lee, J.T. Miller, W.N. Delgass, F. Ribeiro, Water – gas shift catalysis over transition metals supported on

molybdenum carbide, *J. Catal.* 331 (2015) 162–171, <https://doi.org/10.1016/j.jcat.2015.08.017>.

[26] K.D. Sabnis, M.C. Akatay, Y. Cui, F.G. Sollberger, E.A. Stach, J.T. Miller, W. N. Delgass, F.H. Ribeiro, Probing the active sites for water – gas shift over Pt/molybdenum carbide using multi-walled carbon nanotubes, *J. Catal.* 330 (2015) 442–451, <https://doi.org/10.1016/j.jcat.2015.07.032>.

[27] S. Yao, X. Zhang, W. Zhou, R. Gao, W. Xu, Y. Ye, L. Lin, Atomic-layered Au clusters on α -MoC as catalysts for the low-temperature water-gas shift reaction, *Science* 393 (2017) 389–393.

[28] C. Shi, A. Zhang, X. Li, S. Zhang, A. Zhu, Y. Ma, C. Au, Ni-modified Mo₂C catalysts for methane dry reforming, *Appl. Catal. A Gen.* 432 (2012) 164–170, <https://doi.org/10.1016/j.apcata.2012.04.035>.

[29] Q. Bkour, O.G. Marin-flores, M.G. Norton, S. Ha, A highly active and stable bimetallic Ni-Mo₂C catalyst for a partial oxidation of jet fuel, *Appl. Catal. B Environ.* 245 (2019) 613–622, <https://doi.org/10.1016/j.apcatb.2019.01.027>.

[30] T. Iida, M. Shetty, K. Murugappan, Z. Wang, K. Ohara, T. Wakihara, Y. Román-Leshkov, Encapsulation of molybdenum carbide nanoclusters inside zeolite micropores enables synergistic bifunctional catalysis for anisole hydrodeoxygénéation, *ACS Catal.* 7 (2017) 8147–8151, <https://doi.org/10.1021/acscatal.7b03175>.

[31] X. Zhang, M.E. Reece, C.B. Cockreham, H. Sun, B. Wang, H. Xu, J. Sun, X. Guo, H. Su, Y. Wang, D. Wu, Formation energetics and guest–host interactions of molybdenum carbide confined in zeolite Y, *Ind. Eng. Chem. Res.* 60 (2021) 13991–14003, <https://doi.org/10.1021/acs.iecr.1c02822>.

[32] Z. Li, C. Chen, E. Zhan, N. Ta, Y. Li, W. Shen, Crystal-phase control of molybdenum carbide nanobelts for dehydrogenation of benzyl alcohol, *Chem. Commun.* 50 (2014) 4469–4471, <https://doi.org/10.1039/c4cc00242c>.

[33] Y. Chen, B. Qiu, Y. Liu, Y. Zhang, An active and stable nickel-based catalyst with embedment structure for CO₂ methanation, *Appl. Catal. B Environ.* 269 (2020), 118801, <https://doi.org/10.1016/j.apcatb.2020.118801>.

[34] F. Okuyama, Y. Fujimoto, S. Kato, T. Kondo, Growth of molybdenum carbide particles from an amorphous phase induced by ion bombardment, *Appl. Phys. A Solids Surf.* 38 (1985) 275–279, <https://doi.org/10.1007/BF00616063>.

[35] J.M. McEnaney, J. Chance Crompton, J.F. Callejas, E.J. Popczun, A.J. Biacchi, N. S. Lewis, R.E. Schaak, Amorphous molybdenum phosphide nanoparticles for electrocatalytic hydrogen evolution, *Chem. Mater.* 26 (2014) 4826–4831, <https://doi.org/10.1021/cm502035s>.

[36] C.H. Bartholomew, Sintering kinetics of supported metals: new perspectives from a unifying GPLE treatment, *Appl. Catal. A Gen.* 107 (1993) 1–57, [https://doi.org/10.1016/0926-860X\(93\)85114-5](https://doi.org/10.1016/0926-860X(93)85114-5).

[37] J. Sehested, J.A.P. Gelten, I.N. Remediakis, H. Bengaard, J.K. Nørskov, Sintering of nickel steam-reforming catalysts: effects of temperature and steam and hydrogen pressures, *J. Catal.* 223 (2004) 432–443, <https://doi.org/10.1016/j.jcat.2004.01.026>.

[38] Z. Li, X. Hu, L. Zhang, S. Liu, G. Lu, Steam reforming of acetic acid over Ni/ZrO₂ catalysts: effects of nickel loading and particle size on product distribution and coke formation, *Appl. Catal. A Gen.* 417–418 (2012) 281–289, <https://doi.org/10.1016/j.apcata.2012.01.002>.

[39] Y. Cui, H. Xu, Q. Ge, Y. Wang, S. Hou, W. Li, Structure sensitive dissociation of CH₄ on Ni/ α -Al₂O₃: Ni nano-scale particles linearly compensate the E_a and lnA for the CH₄ pulse kinetics, *J. Mol. Catal. A Chem.* 249 (2006) 53–59, <https://doi.org/10.1016/j.molecata.2006.01.009>.

[40] M. Xu, J.A. Lopez-Ruiz, L. Kovarik, M.E. Bowden, S.D. Davidson, R.S. Weber, I. W. Wang, J. Hu, R.A. Dagle, Structure sensitivity and its effect on methane turnover and carbon co-product selectivity in thermocatalytic decomposition of methane over supported Ni catalysts, *Appl. Catal. A Gen.* 611 (2021), 117967, <https://doi.org/10.1016/j.apcata.2020.117967>.